Draft version May 17, 2020
Typeset using LaTeX **twocolumn** style in AASTeX63

Microlensing by Galactic Center SMBH

Yi-Xian Chen[1,2] and Jessica R. Lu[1]

[1] *Department of Astronomy, University of California, Berkeley, CA, USA*
[2] *Department of Physics, Tsinghua University, Beijing, China*

Submitted to ApJ

ABSTRACT

We re-examine the rate of microlensing events produced by the Supermassive Black Hole (SMBH) at the Galactic Center as a fixed lens, based on the methods given by Alexander & Sternberg (1999) and Alexander & Loeb (2001). By applying updated observational constraints for the distribution of stars within < 20pc of the SMBH, we estimate the lensing rate for two scenarios, i) the lensing rates of *local stellar sources* by the SMBH and ii) the enhancement by surrounding stars as secondary lenses, of lensing events of *distant background sources* by the SMBH. From our results, we predict the K-band microlensing rates or optical depths of such events and bridge the gap between situations i) and ii). We find our new results to be generally consistent with these previously published references. For the local stellar source microlensing, we obtained an event rate of $\Gamma = \tau/\bar{t} = 9 \times 10^{-3}\mathrm{yr}^{-1}$ for an observational threshold of 19 mag where τ is the source optical depth and $\bar{t}$ is the average timescale; For the enhanced lensing of background stars, we predict that that in any snapshot of the central $2'' - 3''$ region taken with a modern detection threshold of 21 mag, $\sim 2\%$ of total background stars will be amplified for more than 500% in brightness, twice the value compared to SMBH single-lens optical depth. As more potential microlensing events in the GC are being identified by AO surveys with a much higher precision than previous speckled observations, we would be able to test our predictions and offer implications on the theoretical models of GC and the SMBH.

Keywords: Gravitational microlensing (672), Galactic center (565), Supermassive black holes (1663), Binary lens microlensing (2136)

1. INTRODUCTION

Over the past two decades, high-resolution infrared observations of the Galactic Center (GC) and the region around Sgr A* have provided the most precise measurements of a SMBH distance ($D_0 = 7946 \pm 50 \pm 32$pc) and mass ($M_\bullet = 3.964 \pm 0.047 \pm 0.026 \times 10^6 M_\odot$) (Ghez et al. 1998, 2008; Gillessen et al. 2009; Do et al. 2019, for the above result), as well as estimates of the stellar spatial distribution, the K-band luminosity function and kinematics of the stars in the surrounding Nuclear Star Cluster (Schödel et al. 2007; Feldmeier et al. 2014; Fritz et al. 2016; Gallego-Cano et al. 2018; Schödel et al. 2018; Baumgardt et al. 2018; Genzel et al. 2010). Separately, microlensing has been proposed to be an effective means to probe the properties of a dense stellar population (Paczynski 1986, 1996), and numerous campaigns with varied resolutions have also been carried out to identify microlensing events in the Galactic Bulge (Udalski et al. 1993; Alard et al. 1995; Afonso et al. 2003; Sumi et al. 2013; Navarro et al. 2017). However, these low-resolution microlensing surveys, often at optical wavelengths, are unable to probe microlensing events appearing inside the GC and around the SMBH.

In early high-resolution speckle observations of the GC, some variable infrared sources were discovered in the direction of the SMBH (Genzel et al. 1997; Ghez et al. 1998). Alexander & Sternberg (1999, hereafter AS99) proposed that the SMBH could be gravitationally lensing background stars. They calculated the probability of detecting such events in a specific campaign with various intervals between observations. They concluded that the detection rate of such events is quite low but can be made higher if we monitor the GC more frequently with improved sensitivity. Nevertheless, these microlensing rates are higher than or comparable to the rates already observed in the stellar bulges, contributed by regular compact lenses (e.g. Sumi & Penny 2016; Mróz et al. 2019). On the other hand, follow-

up work by Alexander & Loeb (2001, hereafter AL01) showed that lensed images produced by the SMBH lensing a distant background star could be gravitationally lensed themselves by star masses in the vicinity of the SMBH and produce more potentially detectable events. This secondary lensing is analogous to the effect of planets on stellar microlensing signals (Mao & Paczynski 1991; Gould & Loeb 1992) and can produce significantly higher magnification images. The secondary-lensing effect is most pronounced when the second lens is near the Einstein radius of the primary lensing. Relevant studies also proposed that at very close-in distance from the SMBH, stellar-mass black holes (SBH) with masses of typically $> 10M_{\oplus}$ takes up much more fractions of the stellar population due to mass segregation (Alexander & Hopman 2009; Aharon & Perets 2016), than in the galactic bulge where they're relatively loosely scattered (Miralda-Escudé & Gould 2000; Wiktorowicz et al. 2019; Lam et al. 2020). Such SBHs might have a non-negligible contribution in serving as primary (Chanamé et al. 2001) as well as secondary lenses, and could be detected through monitering of enhanced microlensing events in the central parsec.

While more and more non-periodic stellar sources have been discovered in the GC by speckle IR observations afterwards (Rafelski et al. 2007), modern AO studies of stellar variability in the direct GC, with much higher precision to fainter magnitudes, have also been able to identify more variable sources (e.g. Gautam et al. 2019). This suggests that more of such AO surveys could be carried out to probe microlensing events deep in the vicinity of the SMBH. From additional data of potential microlensing events in the future, we would be able to make comparison with predictions of microlensing rate and optical depth calculations to cross-validate the theoretical models of GC and the SMBH.

Since the initial calculations of AS99 and AL01, observational sensitivities have been considerably improved and significant advances have been made in constraining the model of galactic center stellar distributions. In this paper, with a new model of stellar number density, velocity and luminosity distribution obtained from up-to-date observation data of GC stars, we carry out analysis of microlensing events by the SMBH based on previous methodologies, focusing on the main contribution by stars within the central 20 pc. In §2 we will discuss the lensing rate of GC stars as sources amplified by the SMBH, and update the predictions for microlensing rates; in §3 we calculate the contribution of lensing events (optical depth) of distant background stars with local stars acting as secondary lenses, and find the result to be smaller than those of AL01 but generally similar; we will also bridge the gap between the two scenarios by showing that the second case will transform into first case as the sources get closer to the SMBH lens. In §4 we briefly discuss the implication of our results and some future prospects.

2. MICROLENSING OF GALACTIC CENTER STARS BY THE SUPERMASSIVE BLACK HOLE

2.1. *Model Setup*

The Einstein angle is the relative size of the gravitational lensing cross section given by Paczynski (1986)

$$\theta_{\rm E} = \left(\frac{4GM_\bullet}{c^2}\cdot\frac{D_{SL}}{(D_L)(D_{SL}+D_L)}\right)^{1/2} \sim 0.024''\left(\frac{r}{1\ {\rm pc}}\frac{M_\bullet}{4.0\times10^6 M_\odot}\right)^{1/2}. \quad (1)$$

In this context the lens-source distance $D_{LS} = r$, which is defined as the source star's distance from the SMBH along our line of sight, the lens-observer distance $D_L = D_0 = 8$kpc is our distance to Sgr A* and assumed to be 8 kpc throughout this work, $M_\bullet \approx 4.0\times10^6 M_\odot$ is the mass of the supermassive black hole from Do et al. (2019). Measured in angular units, $1'' = 0.039$pc on the lens plane. $R_E = \theta_E D_0$ is the Einstein radius on the lens plane, and the effective lens size at the source plane is $R_S = \theta_E(D_0 + r) \approx R_E$. A more recent fit from Gravity Collaboration et al. (2020) gives a larger estimate of both the SMBH mass and the GC distance ($M_\bullet = 4.26\times10^6 M_\odot, D_0 = 8246.7$pc) which only raises the general normalization for the Einstein angle by 0.1% and the Einstein radius by 3%.

For a source moving at velocity v_{2D} with respect to a fixed lens on the lens plane, it would be able to traverse the projected Einstein radius in the Einstein crossing time

$$t_{\rm E} = R_{\rm S}/v_{2D}, \quad (2)$$

which is analogous to the Einstein crossing time $R_{\rm E}/v_{2D}$ for a moving *lens* with respect to some fixed source. In our context, the range of possible Einstein timescale is quite large, e.g. $t_{\rm E} = 0.08$ yrs for a source located at $r = 0.01$pc with velocity magnitude 1000km/s, while $t_{\rm E} = 20$ yrs for a source at $r = 10$pc crossing with velocity 100km/s.

The dimensionless lens-source separation u is the angular separation of source and lens divided by Einstein angle. While the source is moving across the lens plane, it changes with time in a simple manner

$$u(t) = \sqrt{u_0^2 + \left(\frac{t-t_0}{t_E}\right)^2}, \quad (3)$$

where t_0 is the time of closest approach and u_0 is the closest separation at t_0, also known as the impact parameter. The photometric magnification of the source A changes with time correspondingly through its relation with u:

$$A(u)u\sqrt{u^2+4} = u^2+2. \tag{4}$$

Generally the magnification increases with closer separation, resulting in a maximum magnification at $u = u_0$. At small separation, $A \sim 1/u$.

A gravitationally lensed point source produces one image within and one outside the Einstein ring. The angular separation between the two images is

$$\Delta\theta = \theta_{\rm E}\sqrt{u^2+4} \sim 2\theta_{\rm E} \quad (\text{for } u \lesssim 1). \tag{5}$$

Generally when $\Delta\theta/2$ is smaller than ϕ, the FWHM angular resolution of the observations, the two images cannot be resolved and the source will appear as a resolved lensing event.

The required total source amplification for a star to be detected, dependent on observation condition and the star's luminosity, yields to

$$A_{min}(K_s; K_0) = 10^{-0.4(K_0-K_s)}, \tag{6}$$

where K_s is the raw apparent magnitude and K_0 is the detection threshold.

The maximum impact parameter of a microlensing event is therefore given by:

$$u_{max}^2 = \frac{2A_{min}(K_s;K_0)}{\sqrt{A_{min}(K_s;K_0)^2-1}} - 2. \tag{7}$$

The difference in source luminosity leads to the classification of "faint-star lensing" and "bright-star lensing". For faint stars with an unlensed apparent magnitude $K_s \gtrsim K_0$, it is only upon entering a circular region with angular radius $u_{max}\theta_{\rm E}$ where $u_{max} \leq 1$ that it can be detected via microlensing. For bright stars with $K_s \lesssim K_0$, however, they can already be identified without the aid of lensing and the lensing event itself would be characterized by the rise in magnification above order unity rather than the appearance of the source. To prevent divergence in u_{max}, we artificially set u_{max} to 1 for bright stars and the corresponding magnification threshold for such an event will be $A_{min}(K_s; K_0) = 1.34$.

The microlensing timescale for stars with maximum impact parameter u_{max} at source-lens distance r is therefore generally expressed as

$$t = \frac{2R_S\sqrt{u_{max}^2-u_0^2}}{v_{2D}} = 2t_E\sqrt{u_{max}^2-u_0^2}, \tag{8}$$

which is the appearance timescale for faint stars but the *amplification* timescale for bright stars.

The total integrated rate for microlensing above the given threshold K_0 is given by:

$$\begin{aligned}\Gamma(K_0) =& 2\langle u_{max}\rangle \int_{r_1}^{r_2} R_{\rm S}(r)\overline{v_{2D}}(r)n_*(r)dr \\ \approx& 2\langle u_{max}\rangle \int_{r_1}^{r_2} R_{\rm E}(r)\overline{v_{2D}}(r)n_*(r)dr.\end{aligned} \tag{9}$$

In our notation, any luminosity-related quantity averaged over luminosity distribution is denoted by $\langle\rangle$, i.e.

$$\langle X(L_K)\rangle = \int X(L_K)df(L_K), \tag{10}$$

where $df(L_K)$ is the number fraction of stars within a specific luminosity bin. n_* is the total number density of stars that are effective sources of K-band luminosity, and $\overline{v_{2D}}$ is the 2-dimensional velocity perpendicular to line of sight averaged over the velocity distribution, both assumed to be functions of source-lens distance r in the small angular area directly behind the SMBH. Note that the for continuous monitering (assuming a microlensing event can be detected with 100% efficiency no matter how short its timescale is), the local rate for stars of fixed distance and luminosity averaged over a uniform distribution of impact parameter, is going to be

$$\begin{aligned}\frac{d^2\Gamma}{drdf} &= 2u_{max}(K_s)R_{\rm S}n_*\overline{v_{2D}} \\ &\approx 2u_{max}(K_s)R_{\rm E}n_*\overline{v_{2D}},\end{aligned} \tag{11}$$

associated with the total stellar *number* flux over a magnification cross section, rather independent of the duration of each specific event (Peale 1998; Mróz et al. 2019). In this expression, only u_{max} has a luminosity dependence, ergo this integration (averaging) can be taken out separately in Eqn 9. The differential formula can be derived following the conventional rules from Paczynski (1986) of $\Gamma = \frac{\tau}{\bar{t}}$ where τ is the optical depth of events (in some cases multiple lenses corresponding to a fixed source, while in this case multiple sources with a fixed lens) and $\bar{t}$ is the mean event timescale of all the events concerned. We have also provided a new interpretation elaborated in Appendix A.

In this paper, we focus on stars within < 20pc which contributes the bulk of stellar population in the galactic center and for which we have a specific model. In fact, from AS99's results it also follows that the microlensing rate due to stars in the nearest 10pc dominates the total rate. Therefore, we choose $r_2 = 20$pc, the outer boundary of our updated stellar model, as our integration upper limit in Eqn 9. In 7 we show that the differential microlensing rate contributions outside 20pc is very

small, and the result should be insensitive of r_2. The lower limit is $r_1 = 0.003$pc which is the mean central stellar separation (see §2.6).

2.2. *K Luminosity Function*

As shown in Eqn 9, in integration of luminosity-related quantities like $u_{max}(K_s; K_0)$, we have to take in different contributions from a range of luminosity bins. This probability distribution is given by the K luminosity function. Blum et al. (1996) shows that it does a reasonable job to fit the K Luminosity distribution (number fraction) with a power law

$$df(L_K) \propto L_K^{-\beta} \tag{12}$$

where $\beta \sim 2$.

In practice, we adopt a normalized KLF of the central region of Galactic Center from Gallego-Cano et al. (2018) that accounts for the older, late-type stellar population and extrapolate the profile to an assumed cutoff at 21.5 mag. The adopted KLF is shown in Fig 1, with binsize 0.25 mag ranging from 9.5-21.5 mag.

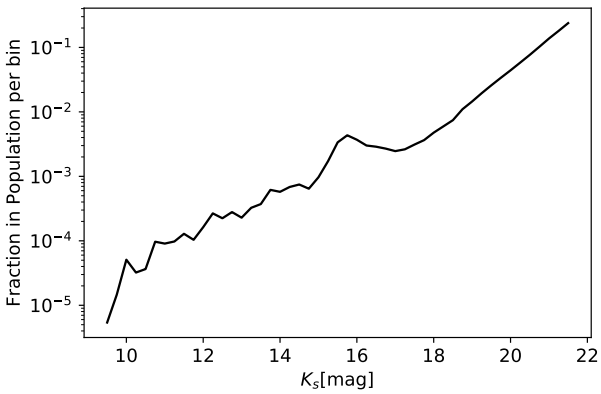

Figure 1. Our adopted K-band luminosity function from 9.5-21.5 mag. The model from K=9.5-18.5 is from (Gallego-Cano et al. 2018) and the fainter bins were extrapolated using a power-law of $df(L_K) \propto L_K^{-2.2}$.

2.3. *Number Density Function*

In Eqn 9 we also need the number density of stars at specific distance to calculate the lensing flux/rate. The 3D number density of K-band stars in the nuclear cluster can be fit by a Nuker model (done in Gallego-Cano et al. (2018); Schödel et al. (2018)), representing a typical broken power-law function (Lauer et al. 1995):

$$n_*(r) = n_*\,(r_\mathrm{b})\,2^{(\beta-\delta)/\alpha}\left(\frac{r}{r_\mathrm{b}}\right)^{-\delta}\left[1+\left(\frac{r}{r_\mathrm{b}}\right)^{\alpha}\right]^{(\delta-\beta)/\alpha}, \tag{13}$$

which is more realistic than the isothermal law derived by Genzel et al. (1996, 1997) in our regions of focus.

Generally, the GC does not show strong evidence for a luminosity dependent density profile for K-band sources (Schödel et al. 2018; Baumgardt et al. 2018). We therefore adopt a profile taken from Gallego-Cano et al. (2018) for stars within 17.5-18.5 mag (see their Fig. 14), and normalize it according to our KLF. This model has a break radius of $r_b = 4.9 \pm 0.5$pc and $\delta = 1.42 \pm 0.03, \beta = 3.5 \pm 0.3$ which yields a 3D stellar density at the break radius of $n_*(r_b) = 3354\mathrm{pc}^{-3}$. The sharp parameter α is set to 10 and does not have any significant impact on the other best fit parameters. This profile of the GC is generally in agreement with the fit from Schödel et al. (2007). Schödel et al. (2018) gives a flatter fit with $\gamma \approx 1.15$ which could be accounted by systematic biases related to different methods.

The projected surface density Σ_* is related to the 3D number density by integration:

$$\Sigma_*(r) = 2\int_r^\infty \frac{x n_*(x)\mathrm{d}x}{\sqrt{x^2-r^2}}. \tag{14}$$

The plotted distributions are as shown in Figure 2.

The young stars relatively small in numbers compared to the old giants ($\lesssim 5\%$ of the population) generally follow a steeper power law distribution more consistent with the BW cusp (Bahcall & Wolf 1976), without flattening towards the central parsec. However, the rise in their number density within central region is still not significant enough to affect the total rate on an integrated scale (Eisenhauer et al. 2005; Schödel et al. 2007; Lu et al. 2009; Støstad et al. 2015). Moreover, their numbers follow a somewhat Top Heavy Model in luminosity function (Bartko et al. 2010; Pfuhl et al. 2011; Do et al. 2013; Lu et al. 2013) that *doesn't* increase sharply after extrapolation towards lower luminosity region, making up even smaller fraction as far as we are concerned. Therefore, we will exclude them from our modeling.

2.4. *Velocity Distribution*

We use the data from Feldmeier et al. (2014); Chatzopoulos et al. (2015) which has less outliers and extreme velocities than previous observations (e.g. McGinn et al. 1989) to derive our model for velocity distribution. First, we use python curve_fit to fit an azimuthally averaged logarithmic function for the 2-D velocity profile, assuming the rotation velocity is perpendicular to the line of sight (AS99). The fitted velocity distribution is:

$$v_\mathrm{rot}(r) = 54.4 + 17.9\log_{10}(r/1\mathrm{pc})\ \mathrm{km\ s^{-1}}. \tag{15}$$

For the Gaussian dispersion, we perform a fit on the data in the basic form $\sigma(r) = [A^2 + B^2 r^{-C}]^{1/2}$ derived

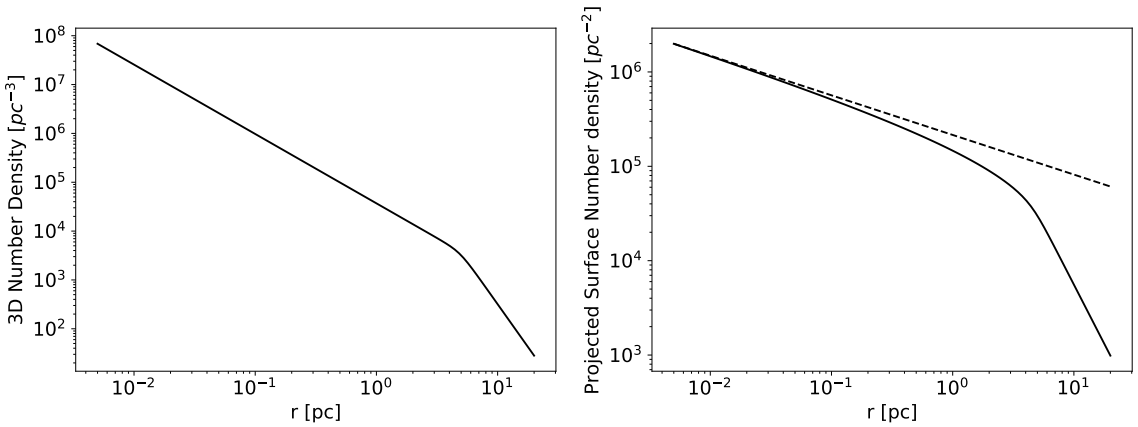

Figure 2. Isotropic Nuclear Star Cluster stellar population model. Left: number density of K-emitters with respect to distance from GC according to fitted Nuker model and KLF from Gallego-Cano et al. (2018) in black bold lines; Right: Corresponding projected surface number density of K-emitters, with an asymptotic profile $n_* \propto r^{0.42}$ at small r indicated with a dotted line which we will make use of in Section 3

by Genzel et al. (1996) based on an isotropic model to obtain some relatively accurate fits:

$$\begin{aligned}\sigma_l(r) &= [97.7^2 + 25.5^2(r/1\mathrm{pc})^{-1.35}]^{1/2}\ \mathrm{km\ s^{-1}},\\ \sigma_b(r) &= [59.2^2 + 58.4^2(r/1\mathrm{pc})^{-0.80}]^{1/2}\ \mathrm{km\ s^{-1}}.\end{aligned} \tag{16}$$

Assuming $\sigma^2 = \sigma_l^2 + \sigma_b^2$ in the full model, we plot the rotational velocity as a function of r with dispersion magnitude in the form of errorbars in Figure 3. The two-dimensional distribution function of the projected velocity in polar coordinates is

$$DF_2\left(v_{2D}\right) d^2 v_{2D} = \frac{\hat{v}_{2D}}{2\pi} e^{-\frac{1}{2}\left(\hat{v}_{2D}^2 + \hat{v}_{\mathrm{rot}}^2 - 2\hat{v}_{2D}\hat{v}_{\mathrm{rot}}\cos\theta\right)} d\hat{v}_{2D} d\theta \tag{17}$$

where $\hat{v}_{2D} = v_{2D}/\sigma$, $\hat{v}_{rot} = v_{rot}/\sigma$, and θ is an evenly distributed angle between $\vec{v_{2D}}$ and $\vec{v_{rot}}$. The average 2D velocity over all possible $\vec{v_{2D}}$ gives $\overline{v_{2D}}(r) = v_{rot}(r)$.

2.5. *Cumulative Lensing Rate for Long and Short Timescales*

Eqn 9 corresponds to *continuous monitoring*. However, the realistic event rate changes when the observing interval ΔT alters since those sources with timescale $t < \Delta T$ may fall outside the survey window into observing gaps.

As an example, consider a monitoring campaign that consists of a series of n very short observing runs that are carried out during a total time period T (typically $T \sim$ several years), with a mean interval ΔT between each observing run (typically $\Delta T \sim$ a month to a year). We wish to distinguish between long and short events, where the long events have $t > \Delta T$ and would be detected as a time-varying source with efficiency $\eta_{long} = 100\%$; and the short events with $t < \Delta T$ would *probably* appear as a momentary event inside one of n runs with lower efficiency $\eta_{short} = t(< \Delta T)/\Delta T$. In the limit of small event rates, the total detection probability may be written as:

$$\begin{aligned}P = P_{\mathrm{short}} + P_{\mathrm{long}} &= n\bar{t}_{\mathrm{short}}\,\Gamma_{\mathrm{short}} + T\,\Gamma_{\mathrm{long}}\,,\\ \Gamma_{\mathrm{short}} + \Gamma_{\mathrm{long}} &= \Gamma_{\mathrm{total}},\end{aligned} \tag{18}$$

with the rate for "long" microlensing events Γ_{long} approaching the total rate Γ_{total} for continuous monitoring ($\Delta T = 0$). Long events that can be detected with 100% efficiency have a timescale t longer than

$$t = \frac{2R_S\sqrt{u_{max}^2 - u_0^2}}{v_{2D}} > \Delta T. \tag{19}$$

This yields an upper limit to the velocity that depends on the observation interval ΔT, source luminosity L_K, distance r *and* and impact parameter u_0,

$$v_c = 2\left(u_{max}^2 - u_0^2\right)^{1/2} R_S/\Delta T. \tag{20}$$

As sources with velocity lower than this critical value have a duration that exceeds the observational interval, the differential rate of *long timescale* events for certain $u_{max}(L_K)$ and $R_S(r)$ but averaged over impact parameter and velocity distribution, would be

$$\frac{d^2\Gamma_{long}}{dr\,df} = 2R_{\mathrm{s}}n_* \int_0^{u_{max}} du_0 \int_0^{v_c} v_{2D} DF_2\left(v_{2D}\right) d^2 v_{2D}, \tag{21}$$

Calculation of the rate-averaged amplification $\Delta K(> \Delta T)$ follows a similar rule. The local impact parameter u_0 weighted with local lensing rate Γ is given by

$$\begin{aligned}u_0\frac{d^2\Gamma_{long}}{drdf} &= 2R_{\mathrm{s}}n^* \int_0^{u_{max}} u_0 du_0\\ &\times \int_0^{v_c} v_{2D} DF_2\left(v_{2D}\right) d^2 v_{2D},\end{aligned} \tag{22}$$

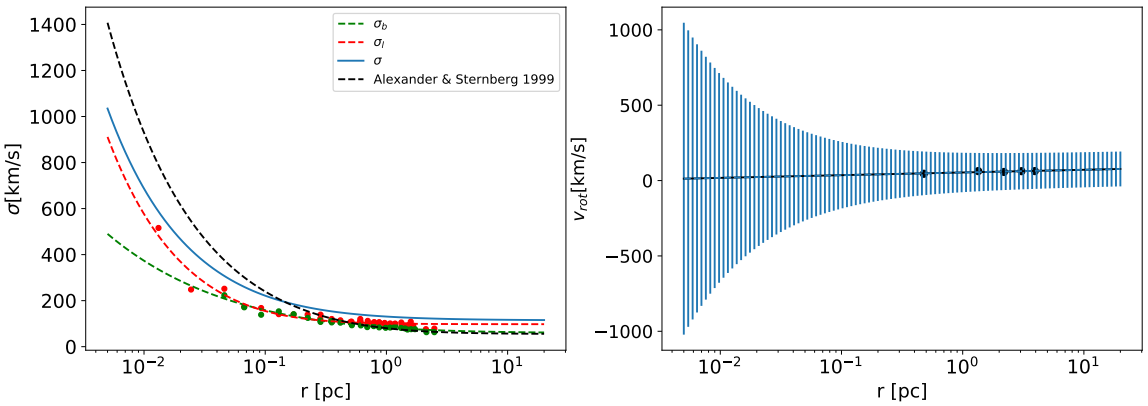

Figure 3. Left: Fitted dispersion distribution of $\sigma_b(r), \sigma_l(r)$ and total $\sigma(r)$; Right: 2-D Velocity distribution, the solid black line is the mean profile $v_{2D}(r)$, vertical bars denoting the magnitude of Gaussian dispersion. Dots with corresponding colors are data points used for fitting, errorbar of the data points see Feldmeier et al. (2014); Chatzopoulos et al. (2015)

so the total rate-averaged impact parameter is

$$\overline{u}_0(>\Delta T) = \frac{\int_{r_1}^{r_2}\int_{L_K} u_0 \dfrac{d^2\Gamma_{long}}{drdf}}{\Gamma_{long}(>\Delta T)}, \tag{23}$$

and the median amplification above threshold is $\overline{A} = \langle u_{max}\rangle/\overline{u_0}$. Mathematically, by using some simplified forms of these integrals derived by AS99, it is easy to show that as ΔT approaches zero, $\overline{A}$ approaches 2, and $\overline{\Delta K}(>\Delta T) = 2.5\log\overline{A}$ approaches 0.75.

Calculation of rate-average timescale of short events with $t < \Delta T$ is again similar. The local impact timescale weighted with local lensing rate is given by

$$\begin{aligned} t\frac{d^2\Gamma_{short}}{drdf} = 4R_S^2 n^* \int_0^{u_{max}} \sqrt{u_{max}^2 - u_0^2}\, du_0 \\ \times \int_{v_c}^{\infty} DF_2\left(v_{2D}\right) d^2 v_{2D}, \end{aligned} \tag{24}$$

and therefore the rate-averaged time scale

$$\bar{t}(<\Delta T) = \frac{\int_{r_1}^{r_2}\int_{L_K} t\dfrac{d^2\Gamma_{short}}{drdf}}{\Gamma_{short}(<\Delta T)} \tag{25}$$

would be to average the local timescale over luminosity distribution and distance r.

We have separated the lensing events into two categories: long and short. Furthermore, we should divide them into *resolved* and *unresolved* imaging in calculation.

2.6. *Resolved and Unresolved Imaging*

The lensing events farther away from the SMBH have larger Einstein Angle, and therefore are more likely to be resolved. According to AS99, the maximal lens-source distance for the two lensing images to be unresolvable is about:

$$r_\mu = \frac{(D_0/8\mathrm{kpc})^2}{M_\bullet/(4.0\times10^6 M_\odot)}\left(\frac{\phi}{0''.0145}\right)^2 \mathrm{pc}, \tag{26}$$

where $\Delta p\left(K_0\right)$ is the mean projected angular separation between the observed stars corresponding to $S_0 = \Delta p\left(K_0\right)^{-2}$, where S_0 is the central surface density of stars where the images will appear, and $\phi = \Delta p\left(K_0\right)/\sqrt{\pi}$ is the FWHM angular resolution of the observations required to detect the lensed star.

One problem with Nuker fit is that the power γ makes the surface density diverge to very high values when r reaches the exact center. This can be reconciled by taking the surface density at $\sim 1''$ to represent S_0 since most AO analyses can only reliably determine surface densities for bins on the order of $\gtrsim 1''$ (Baumgardt et al. 2018; Schödel et al. 2018). This means the central surface density detected by a survey with threshold magnitude K_0 would be:

$$S_0(K_0) \approx \Sigma_*\left(1''\right) \times [\text{fraction of stars with } K_s < K_0]\,. \tag{27}$$

This formula gives a central surface number density of $\sim$ 60 per square arc-second for stars with $K_s < 18.5$ mag and 30 per square arc-second for stars with $K_s < 17$ mag. It follows from this concern that we only integrate stars with $r > r_1 = 0.003$ pc in Eqn 9 since 0.003pc is the stellar separation calculate from the *total* K-band surface density at 1". This is modestly smaller than the lower limit $r_1 = 0.005$pc used in AS99.

When $r > r_\mu$ (beyond which distance the contribution to the lensing event rate is already quite low), the two lensing images will appear at an offset of $\sim 2\theta_E$ on

opposite sides from the central lens as commonly seen in strong lensing events (Wardle & Yusef-Zadeh 1992; Dong et al. 2019), and each image will produce an independent characteristic light curve. AS99 suggested that the fractional event lensing rate of these events could be calculated with a modified effective amplification $A' = A/2$. While this is an approximation, it is always valid for relatively high amplification since for the two splitted images we always have $|A_1 - A_2| = 1$. Generally, these events are harder to detect, but if both images are observed, the identification of the event as lensing will be much more certain. So practically we divide the sources into two populations, depending on distance, and calculate the resolved and unresolved rates separately with different effective amplification. The critical distance with which we divide the two populations r_μ exists within our integration range of < 20pc only for very sensitive luminosity thresholds $K_0 = 20, 21$mag, which may be reachable within 1" with the Thirty-Meter-Telescope (Schöck et al. 2009). For even smaller binsize than $\sim 1''$, the critical distance would be smaller.

It is to be noted that since any unresolved image cannot be separated from its corresponding image located at a distance of $\sim 2\theta_{\rm E}$, therefore it cannot be directly separated from Sgr A* itself located at a distance of $\sim \theta_{\rm E}$. However, as AS99 has implied, these lensing events are likely to appear in the form of Sgr A* variability with lack of radio and X-ray counterparts, making themselves distinguishable from the usual Sgr A* flares as results of accretion scenarios. The lightcurves of such variability can then be closely examined for resemblance of a lensing event.

2.7. *Results*

Our results for the new models are presented in Fig 4, 5 & 6.

In the left panels, we plot the cumulative lensing rates for all events with duration t longer than the detection interval ΔT as a function of ΔT. Naturally, the long event cumulative lensing rate would decrease as the observation interval grows larger as smaller fractions of the lensing events satisfy $t < \Delta T$. As ΔT approaches 0, Γ_{long} (resolved+unresolved) approaches its asymptotic value of total lensing rate. The total lensing rate for $K_0 = 17$mag, for example, is calculated to be 2×10^{-3} per year, smaller compared to 3×10^{-3} of AS99. Although the different KLF we adopted from observation which puts more weight in the brighter population gives a mean impact parameter $\langle u_0 \rangle$ larger than theirs, this effect is overcome by our mean velocity profile being generally lower, ergo we have a smaller rate.

As the threshold rises from 17-20 mag, the unresolved lensing rate also rises and it contributes the bulk of the lensing rate just as predicted in AS99, since the critical resolving radius d_μ is quite large (18 pc for $K_0 = 20$ mag and well beyond the integration outer boundary for lower magnitude thresholds). However, when the threshold reaches 21 mag, d_μ reduces to ~ 2 pc, so the contribution by unresolved events decrease abruptly and a larger number of images would be resolved.

In the right panels of Fig 4 & 5, we plot $\overline{\Delta K}(> \Delta T)$, the rate-averaged (maximal) amplification for long events. As sampling interval ΔT increases, the longer timescale events are more likely to be contributed by stars that come closer to the SMBH, resulting in its rise from the asymptotic value of 0.75 mag (which should be the total-rate averaged mean). This effect is less pronounced for bright-star and resolved lensing since the majority of events are contributed by long timescale ones. Generally, our typical amplification is larger than AS99 since long events are rarer to happen and on the whole require closer lens-source distance, and the median amplification converges more slowly to 0.75 mag at small intervals. This is because our Nuker model of stellar density naturally means that stars closer to the black hole gets a higher density weight in rate contribution, while the isothermal profile used by the previous reference doesn't (See Fig 9). For an interval of $\Delta T = 1$yr and a detection threshold of 19 mag, the characteristic amplification would be $\overline{\Delta K} \sim 1$mag.

In Fig 6 we plot the rate-averaged lensing time-scale, $\overline{t_{short}}$ for events with $t < \Delta T$. This averaged value is almost insensitive to K_0, and for very short ΔT it approaches $\Delta T/2$ which gives us a rate that's independent to the timescale.

We notice that the results for bright star imaging is sensitive to our artificial cutoff value of A and the there tends to be numerical instabilities in small ΔT regions for the calculation of $\overline{t_{short}}$, this was also made clear by AS99. To avoid complications, in table we summarize how exactly we are categorizing the different rate calculations.

After obtaining this information, we will be able to use Eqn 18 to calculate the probability of detecting a lensing event for a given total time T, observation timescale of one run ΔT, and number of observations n. For example, for $K_0 = 19$ mag, $\Delta T = 1$yr, $n = 10$, from summing up the bright star and faint star lensing rate from $\Delta T \to 0$ asymptotic values in the left panel of Fig 4, we have $\Gamma_{total} \approx 0.009\text{yr}^{-1}$. Then, by summing up the lensing rate corresponding to $\Delta T = 1$yr we have $\Gamma_{long} \approx 0.005\text{yr}^{-1}$ and therefore $\Gamma_{short} \approx 0.004\text{yr}^{-1}$. Finally from Fig 6 we see $\overline{t_{short}} \approx 0.2$yr, so we have a total

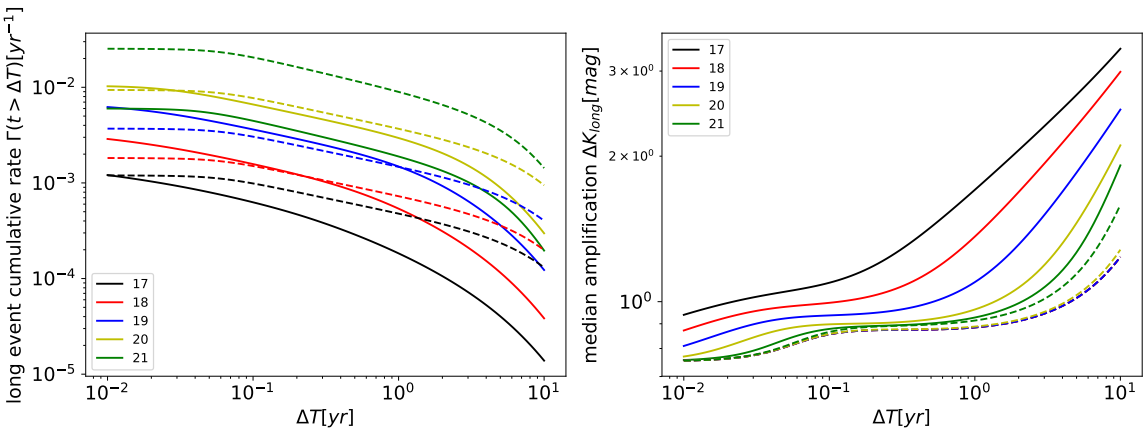

Figure 4. The cumulative long timescale event (events with duration $t > \Delta T$) lensing rate $\Gamma(> \Delta T)$, and the rate-averaged amplification $\overline{\Delta K}(> \Delta T)$ as functions of the sampling interval ΔT for *unresolved* lensing, detection thresholds $K_0 = 17$, 18, 19, 20 and 21 mag, as functions of the sampling interval ΔT. Bold lines show results for faint-star lensing and dotted lines for bright-star lensing corresponding to the bold line of same color. The rates decrease from its asymptotic value of $\Gamma_{total} = \Gamma_{long}(\Delta T \to 0)$ as the sampling interval increases.

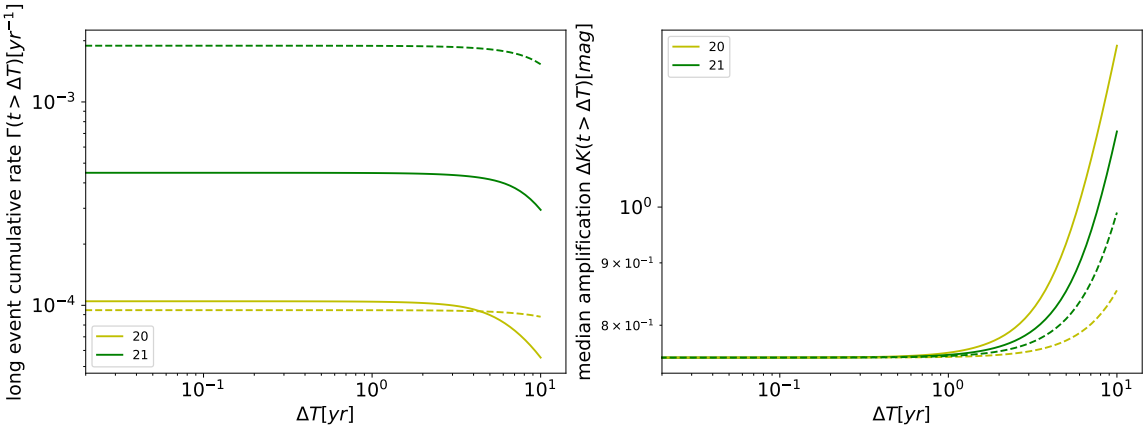

Figure 5. The cumulative long timescale event lensing rate and the rate-averaged maximum amplification in magnitude for *resolved* lensing as functions of sampling interval ΔT, notation same as Figure 4. This contribution only exists within our integration limit 20 pc for $K_0 = 20$ and 21 mag detection thresholds.

Table 1. Categorization of different lensing events

Parameter				
u_0	Bright-star lensing	$u_0 = 1$	Faint-star lensing	$u_0 < 1$
t	Long-timescale lensing	$t > \Delta T$	Short-timescale lensing	$t < \Delta T$
r	Unresolved lensing	$r < r_\mu$	Resolved lensing	$r > r_\mu$

expected event number of $0.2 \times 10 \times 0.004 + 10 \times 0.005 \approx 0.06$ times.

We also plotted the differential micro-lensing rate as a function of r in Fig 7 for one specific example of $K_0 = 18$ mag and $\Delta T = 1$ yr to show the differential contribution from each radius. We can see that there exists a certain boundary within which the short events contributes most of the lensing rate within ~ 0.1pc. Outside of this boundary, the contribution by short events will reduce to zero. The second break radius of differential long event lensing rate is consistent with the break radius of the Nuker model for stellar density.

3. MICRO-LENSING OF DISTANT SOURCES BY SMBH PERTURBED BY GALACTIC CENTER STARS

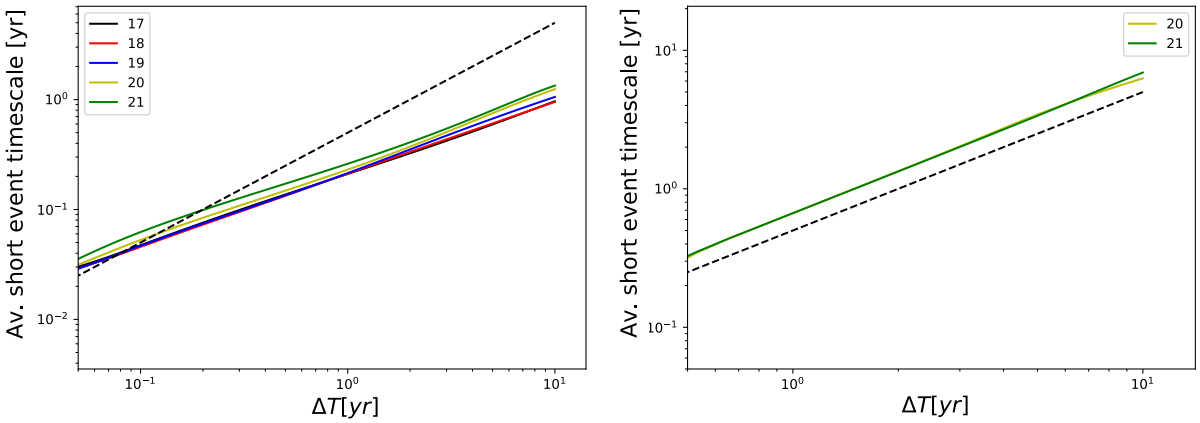

Figure 6. The rate-averaged short lensing timescale, $\bar{t}(< \Delta T)$, as a function of sampling interval ΔT, for unresolved (left panel) and resolved (right panel) lensing. Thin dashed lines show $t = \Delta T/2$.

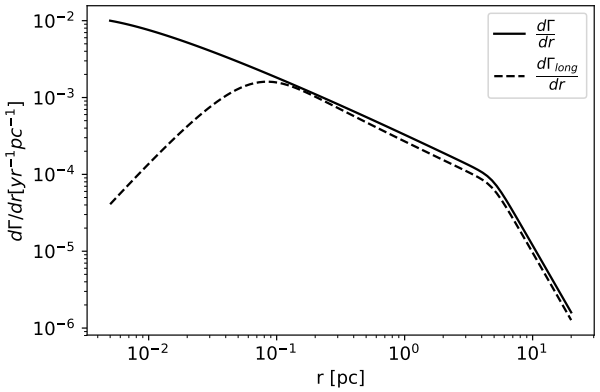

Figure 7. Differential micro-lensing rate as a function of the distance to SMBH for a special case where $K_0 = 18$mag and $\Delta T = 1$ yr. Bold line is total lensing rate (for continuous monitoring) and dotted line shows the rate contributed by long timescale events when the sampling interval is ΔT. Their difference is the contribution from short timescale events.

3.1. *Model Setup*

We next consider microlensing of stellar sources in the *distant background* behind the SMBH rather than in the vicinity of the GC. For such events, the Einstein angle is large enough such that secondary lensing effects must be considered. In this section, we focus on the GC stars in front of the SMBH serving as secondary lenses that can further magnify a source image produced by SMBH primary lensing. In other words, the SMBH produces lensed images of a background source that become the source for a second lensing event from a foreground GC star. For these more distant background sources, $r \sim D_0$ instead of $r \ll D_0$; thus, the Einstein radius should be given by the exact form of:

$$R_E = (1 - \frac{D_0}{r + D_0})^{1/2} R_\infty, \tag{28}$$

or in angular units,

$$\theta_E = \left(1 - \frac{D_0}{r + D_0}\right)^{1/2} \theta_\infty, \tag{29}$$

where

$$\theta_\infty = 2.''02 \left(\frac{M_\bullet}{4 \times 10^6 M_\odot}\right)^{1/2}; R_\infty = D_0 \theta_\infty \tag{30}$$

is the Einstein angle corresponding to a source at infinite distance.

To calculate the effect of GC stars as secondary lenses perturbing the primary image, we consider the model given by Gould & Loeb (1992): The SMBH first magnifies a distant background source in the source plane, forming one of two unperturbed image at (angular) distance x_{BH} to the black hole on the *lens plane* perpendicular to the line of sight. This model assumes that the two unperturbed images are separately resolved and are independent subjects to excess magnification, which is perfectly justified in our large Einstein angle ($\sim 1''$) scenario. We adopt a 2D Cartesian co-ordinate system with the first perturbed image as origin and $\vec{x}_{BH}$ as direction of the x axis. The secondary lens' (GC star's) location is at (ξ_p, η_p) and it projects a perturbed image at (ξ_i, η_i). The unit system is as follows: The unperturbed image distance x_{BH} is expressed in units of $\theta_{\rm E}$, while ξ and η are expressed in units of $\sqrt{\epsilon}\theta_{\rm E}$ where $\epsilon(m) = m/M_\bullet$ is the mass ratio between the secondary and primary lens. The surface area on the lense and source plane calculated are expressed in separate units of $\epsilon\pi\theta_{\rm E}^2$ and $\pi\theta_{\rm E}^2$,

while the stellar densities are also normalized to units of $[\epsilon\pi\theta_{\rm E}^2]^{-1}$ and $[\pi\theta_{\rm E}^2]^{-1}$ so that their product with area gives a dimensionless optical depth.

The position (ξ_i, η_i) are given by 2 or 4 solutions of a quartic equation:

$$\begin{aligned}&\xi_i^4 + \frac{(1-2\gamma)\xi_p}{\gamma}\xi_i^3 \\ &+ \left[\frac{(1-\gamma)^2\left(\xi_p^2+\eta_p^2\right)}{4\gamma^2} - \frac{(1-\gamma)\xi_p^2}{\gamma} - \frac{1}{1+\gamma}\right]\xi_i^2 \\ &- \left[\frac{(1-\gamma)^2\left(\xi_p^2+\eta_p^2\right)\xi_p}{4\gamma^2} + \frac{(1-\gamma)\xi_p}{\gamma(1+\gamma)}\right]\xi_i \\ &- \frac{(1-\gamma)^2\xi_p^2}{4\gamma^2(1+\gamma)} = 0,\end{aligned} \tag{31}$$

where

$$\gamma = x_{BH}^{-2}, \eta_i = \frac{(1+\gamma)\eta_p\xi_i}{2\gamma\xi_i + (1-\gamma)\xi_p}, \tag{32}$$

with the *excess* magnification of each image given by

$$\begin{aligned}A = |1 - &\left[\gamma + (1+\gamma)^2\xi_i^2 - (1-\gamma)^2\eta_i^2\right]^2 \\ &- 4\left(1-\gamma^2\right)^2\xi_i^2\eta_i^2|^{-1}\end{aligned} \tag{33}$$

For a given magnification threshold, we can determine the required area for (ξ_p, η_p) on the lens plane $\sigma_*(>A, x_{BH})$, and the *secondary lens* optical depth $\tau_*(>A, x_{BH}) = \sigma_*(>A, x_{BH})\Sigma_*(x_{BH}) \ll 1$ where Σ_* is the stellar number density at x_{BH}. Because the cross section is small, we neglect any "double" enhancement events where two secondary lenses enter the cross section. In the small optical depth limit, probability of the star being magnified by more than A should be

$$P\left(>A, \boldsymbol{x}_{\rm BH}\right) \simeq \tau_*\left(>A, x_{\rm BH}\right) + \Theta\left(A_{\rm BH} - A\right) \tag{34}$$

Θ is the Heaviside step function and A_{BH} is the magnification by the black hole alone. The form of this probability implies that the bulk of magnification is still provided by the SMBH, and it is only outside the region where the SMBH amplification meets our requirement that the excess magnification of secondary lenses starts to play a role.

Traditionally, we can obtain σ_* by reversely solving the equation, as how Gould & Loeb (1992) gave the equi-magnification contour on the lens plane. However, to give an *area* instead of pinpointing the exact solutions, we can also use Monte Carlo to find the spots for (ξ_p, η_p) that satisfy the magnification constraints. Figure 8 shows some examples of cross-sections generated by Monte Carlo tests.

For exemplary calculation, we assume sources are at a characteristic distance of $D_0 = r$ behind the SMBH which is at our opposite side of the galaxy. The mass ratio is typically $\epsilon = 2.5 \times 10^{-7}$ for a solar-mass star of $m = M_\odot$.

3.2. *Surface Density of Secondary Lenses*

In §2 we have developed a population model of GC that considers the K-band sources, but in the secondary lens surface density, we have to generalize our profile to include the entire stellar population.

We start by assuming that all stars including K-band undetectable ones follow similar power law distribution as Fig 2, and has an average mass of $\bar{m} \sim M_\odot$, so that we can normalize our profile in §2 by fixing the total mass within 1pc to be $1.1 \times 10^6 M_\odot$ (Schödel et al. 2009) to match the observational values. The resulting profile also give a total mass of $8.9 \times 10^6 M_\odot$ within 3.9 pc which matches with Chatzopoulos et al. (2015). This distribution in turn gives us a $\hat{\Sigma}_* = 0.007$ for sources with $r \sim D_0$, smaller than the value 0.04 from AL01.

In Fig 9 we plot our *total* stellar density and those used by AS99, AL01 for comparison. All of whom are obtained applying the assumption $\bar{m} \sim M_\odot$. The isothermal density profile applied by AS99 ignores the inner stellar cusp and AL01's model focuses entirely on the center and ignores the breaking of power law which is completely justified at the typical Einstein radius distance, but still gives a total mass of $3.2 \times 10^6 M_\odot$ within 1 pc which exceeds the observed value significantly. Our model is a combination and a reconciliation of the two.

This stellar surface density function approaches very well to the asymptotic form of $\Sigma_* = \hat{\Sigma}_* x^{-0.42}$ at distance x way within 1 arcsec (e.g. Fig 2), since 0.42 is indeed the asymptotic slope at small r for the integral Eqn 14, where $\hat{\Sigma}_*$ is the normalization factor at $x = \theta_{\rm E}$, Einstein radius of the star, normalized from unit $[\rm pc^{-2}]$ to unit $[\epsilon\pi\theta_{\rm E}^2]^{-1}$. In fact, only the secondary lenses located in a very narrow annulus around the Einstein radius contributes to the enhancement (see Fig 10), therefore we have $\Sigma_* \approx \hat{\Sigma}_*$ in our region of interest and the exact index of the power law is insignificant.

3.3. *Optical Depth on the Lens Plane: Generalized Expressions*

In reality, the mass of stars is not uniformly $M_\odot$, even if we have assumed a mean value of $\bar{m} \approx M_\odot$. Generally, if we have a normalized mass function of the stars $\int g(m)dm = 1$ with relative fractions $g(m)$ not varying much in our relatively small integration range of typically $0.8\theta_E \lesssim x_{BH} \lesssim 1.2\theta_E$ (see Eqn 38), then the optical depth of secondary lenses at a given separation

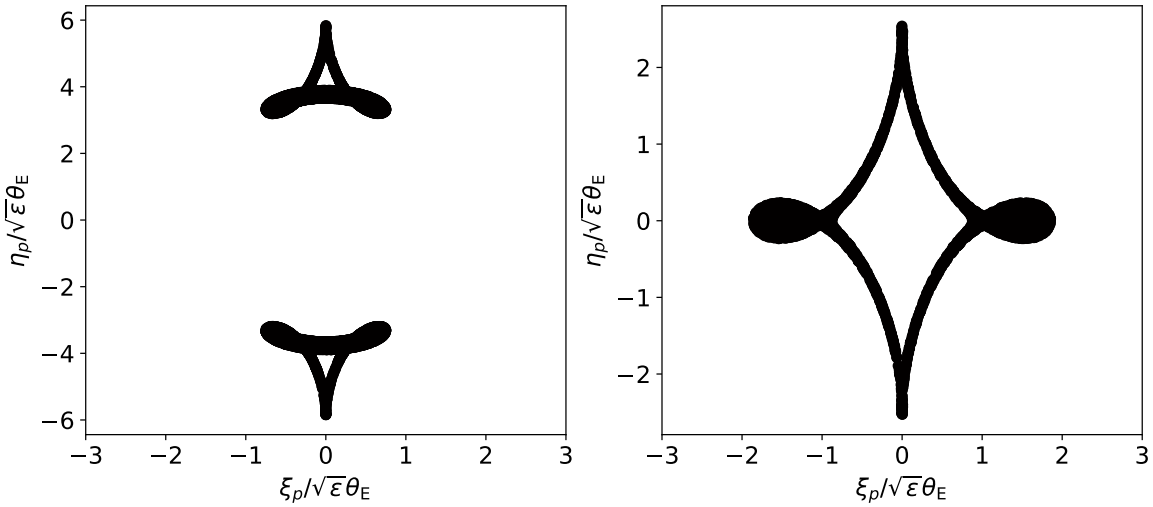

Figure 8. Areas in the (ξ_p, η_p) parameter plane that satisfy the constraint of $A > 300\%$ (for *any* of the perturbed images generated), left panel: $\gamma = 1.3$; right panel: $\gamma = 0.6$. The intrinsic shapes differ for γ larger and smaller than 1, and approaches infinity for γ approaching 1, these images are quite consistent with the contours from (Gould & Loeb 1992)

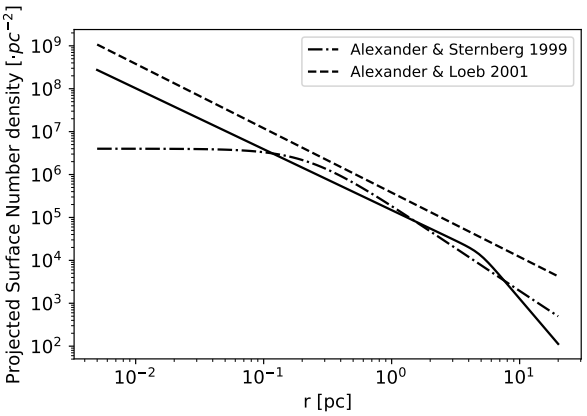

Figure 9. Bold line: the *total* 3D stellar density profile used in Section 3 of our paper. Dotted and dot-dashed lines: the 3D total stellar density profile used by previous references.

from the primary image x_{BH} would be to sum up the surface density from each mass bin $\Sigma_*(x_{BH})g(m)$ normalized from unit [pc^{-2}] to unit $[\epsilon(m)\pi\theta_{\rm E}^2]^{-1}$ multiplied by the corresponding cross section, which always has the same value since it's normalized by default:

$$\begin{aligned}\tau_*(x_{BH}) =&\overline{\Sigma_*(x_{BH})(\epsilon\pi\theta_{\rm E}^2)}\sigma_*(x_{BH})\\ =&\Sigma_*(x_{BH})(\pi\theta_{\rm E}^2)\sigma_*(x_{BH})\int g(m)\frac{m}{M_\bullet}dm\\ =&\Sigma_*(x_{BH})(\pi\theta_{\rm E}^2)\sigma_*(x_{BH})\frac{\bar{m}}{M_\bullet}\\ =&\Sigma_*(x_{BH})(\bar{\epsilon}\pi\theta_{\rm E}^2)\sigma_*(x_{BH}),\end{aligned} \tag{35}$$

Therefore we show that the cross section can be effectively calculated by the mean stellar mass. In §3.2 we assumed $\bar{m} \approx M_\odot$ to constrain the surface number density profiles, therefore we can obtain $\tau_*(x_{BH})$ by simply applying a consistent mean mass ratio of $\bar{\epsilon} = 2.5 \times 10^{-7}$ in rescaling the unit of $\Sigma_*(x_{BH})$.

For an arbitrary $\bar{m}$ and total *mass* surface density of stars $\Sigma_m(x_{BH})$, the total stellar number density would change as $\Sigma_*(x_{BH}) = \Sigma_m(x_{BH})/\bar{m}$, so the total optical depth around x_{BH} is always

$$\tau_*(x_{BH}) \equiv \frac{\Sigma_m(x_{BH})(\pi\theta_{\rm E}^2)\sigma_*(x_{BH})}{M_\bullet}, \tag{36}$$

and only determined by the mass density, which in §3.2 is solely contributed by stars with $\bar{m} \approx M_\odot$ following same power laws. However, GC mass segregation models show that a population of more massive SBHs with $10 - 30M_\odot$ following steeper distribution profiles may take up non-negligible fractions of the stellar number density ($\gtrsim 1\%$) at such close-in distance (Hopman & Alexander 2006; Alexander & Hopman 2009; Aharon & Perets 2016; Emami & Loeb 2020). In principle, a more accurate $\Sigma_m(x_{BH})$ or $\bar{m}$ could be obtained from profiles of segregated stellar species around the Einstein Radius of the SMBH, since they follow different power laws. However, these exact profiles obtained from theoretical mass segregation models are quite dependent on initial assumptions on star formation, therefore we do not invoke any specific models here to calculate the exact value of $\Sigma_m(x_{BH})$ and leave this framework for future study. An accurate $\tau_*(x_{BH})$ is not expected to differ from our results for $\bar{m} \approx M_\odot$ by order unity as

long as such main sequence stars make up the bulk of stellar population. Generally, we point out that for a relatively fixed $\Sigma_m(x_{BH})$ (and therefore fixed $\tau_*(x_{BH})$), it's easy to see that the optical depth contribution from different species scales with the mass fraction. If factor g of number density contributions are from SBHs with mean mass $\bar{m_\bullet} = \mathcal{M}M_\odot$ assuming only two major contributions from stars with average solar mass and SBHs, then contributions from SBHs would take up

$$\frac{\mathcal{M}g}{1-g+\mathcal{M}g} \times 100\% \tag{37}$$

of the total enhanced lensing optical depth $\tau_*(x_{BH})$. If $g = 1\%$ with a medium mass ($\mathcal{M} = 10$) SBH population, this factor would be 9%; For a high mass ($\mathcal{M} = 30$) SBH population, this factor can rise up to 23%, implying a fair possibility for detection SBHs through monitering of enhanced lensing events.

3.4. *Results: Optical Depth of Events on the Source Plane*

Projecting the contribution per annular area on the *lens plane* back onto the *source plane* and assuming an isotropic projected stellar distribution around the black hole, the source plane cross section in our adopted unit system would become:

$$\sigma_s(>A) = 2\int P\left(>A, x_{\rm BH}\right) A_{\rm BH}^{-1}\left(x_{\rm BH}\right) x_{\rm BH} dx_{\rm BH}, \tag{38}$$

where the weight function P is given by Eqn 34, in which the net contribution from secondary lenses is given by Eqn 35. The magnification by SMBH alone is given by

$$A_{\rm BH} = |1 - x_{\rm BH}^{-4}|^{-1}. \tag{39}$$

For background stars within the Einstein angle, there is too much uncertainty in the density and luminosity distribution, so we will compromise with same working model of a large-scale general K Luminosity Distribution as AL01:

$$\Sigma_s(<K_s) = \hat{\Sigma}_s 10^{bK_s}, \tag{40}$$

to account for all sources at a characteristic distance of r from the SMBH, where $\hat{\Sigma}_s = 5\times10^{-10}\left(\theta_{\rm E}(r)/\theta_\infty\right)^2$ and $b = 0.4$. If we assume a luminosity cutoff beyond L_c which corresponds to observed magnitude K_c and amplification cutoff $A_c = 10^{0.4(K_c-K_0)}$, then we can show that if generally $\sigma_s \approx \hat{\sigma_s} A^{-a}$, then the number of lensed images that will be observed, on average, in the inner $2\theta_E$ for limiting magnitude K_0 (namely the *optical depth* τ of events in the source plane) is connected with the source plane cross section by (AL01)

$$\langle\tau\left(>A;K_0\right)\rangle = \int_A^\infty dA' \int_{-\infty}^{K_0} dK \left|\frac{d\sigma_s}{dA}\right|_{A'} \left|\frac{d\Sigma_s}{dK}\right|_{K+K_{A'}}$$
$$= \hat{\Sigma}_s\hat{\sigma}_s\times$$
$$\begin{cases} 10^{bK_c}A_c^{-a} + \frac{a}{2.5b-a}10^{bK_0}\left(A_c^{2.5b-a} - A^{2.5b-a}\right) & A \le A_c \\ 10^{bK_c}A^{-a} & \text{else} \end{cases} \tag{41}$$

The fraction of time that at least one lensing image will be observed (above a certain magnification threshold), corresponding to a Poisson fluctuation, is given by

$$P\left[\tau\left(>A;K_0\right)\ge 1\right] = 1 - \exp\left[-\left\langle\tau\left(>A;K_0\right)\right\rangle\right]. \tag{42}$$

3.5. *Results*

Our integration of contributions from differential annulus in Eqn 38 is carried out from 0.8 to 1.2 for x_{BH}. For a source at distance of typically $r = D_0 = 8$kpc from the lens ($\theta_E \approx \theta_\infty/\sqrt{2}$), the total and differential cross section on source plane will be as shown in Figure 10. The stellar enhancement is lower compared to the results of AL01. Their results shows that for $\theta_E = \theta_\infty$ the cross section follows $\sigma_s \approx 0.35A^{-1.5}$ and the normalization coefficient would be be reduced to 0.16 for $\theta_E = \theta_\infty/\sqrt{2}$, while our result fits with $\sigma_{\rm s} = 0.5A^{-1.8}$ for $\theta_E = \theta_\infty/\sqrt{2}$.

For different θ_E, we find that σ_s with respect to A follow different power laws of power $-2 \sim -1$ with similar normalization constants $\hat{\sigma_s}A$. The net contribution by stars $\sigma_s - \sigma_{s,BH} = \Delta\sigma_s$ is presented in Fig 11. The general profile of $\Delta\sigma_s$ increases as Einstein angle and amplification. If the Einstein radius reduces in length, the $\sigma_s(>A)$ at high magnification will ultimately approach the contribution by Black Hole alone which naturally scale like $A^{-2} \sim u^2 \propto \sigma_{s,BH}$, or more precisely $\sigma_{s,BH} \approx 1/2A^2$ for one of two resolved images when A is bigger than order unity (both σ_s and $\sigma_{s,BH}$ will diverge when A is very small so we do not compare them where $A < 5$). The cross section decreases quickly to the SMBH-only values for sources closer to the SMBH with smaller Einstein radius (E.g when $r \sim 10$ pc, $\theta_{\rm E} \sim 0.03\theta_\infty$), and the situation will gradually transform into the case of GC stars' SMBH-only micro-lensing mechanism discussed in §2, justifying that we do not need to include much secondary perturbation while calculating the lensing rates of GC stars themselves.

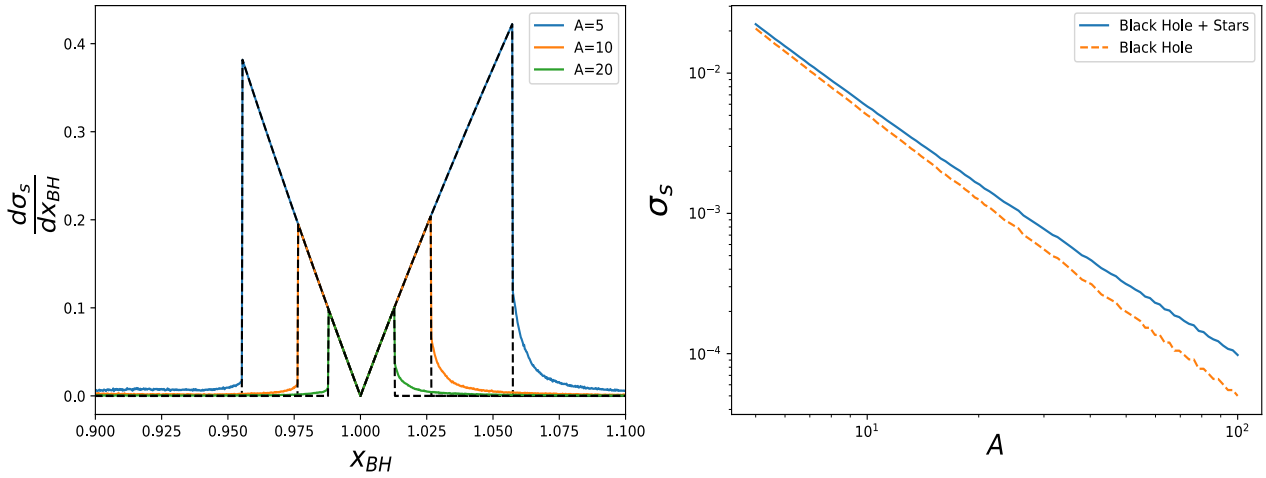

Figure 10. left: The source plane cross section area for a source magnified by more than threshold A contributed by a differential annulus in the lens plane, $\frac{d\sigma_s}{dx_{BH}}$, as a function of angular separation between primary image and SMBH x_{BH}. The case for SMBH+stars (bold lines) is compared to the contribution from the SMBH alone (dashed lines) for three threshold values of A; right: total cross section $\sigma_s(>A)$ as a function of A, for SMBH (dashed line) and SMBH+stars (bold line), integrated from $x_{BH} = 0.85$ to $x_{BH} = 1.20$. Both are for $\theta_E = \theta_\infty/\sqrt{2}$

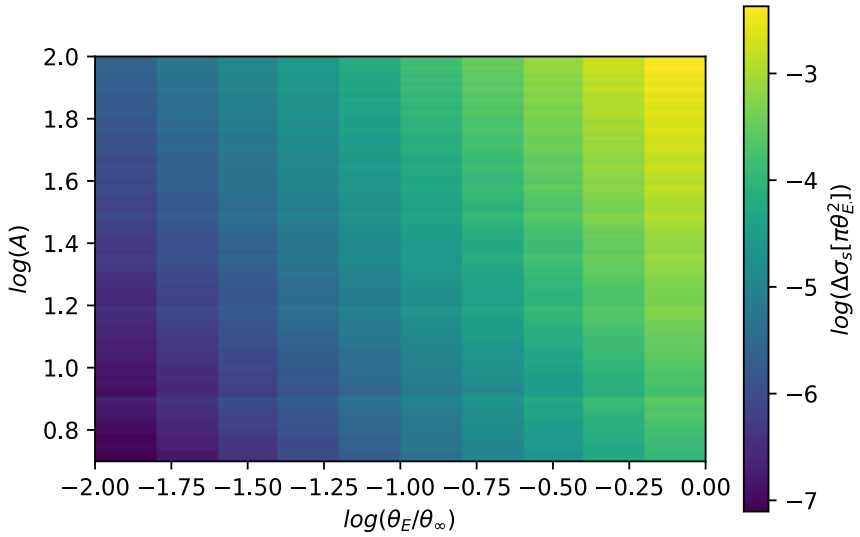

Figure 11. $\Delta\sigma_s(>A)$, the normalized net contribution in magnification cross section by secondary lensing events as a function of Einstein radius and magnification threshold, expressed in unit $[\pi\theta_E^2]$. it follows gradually changing power laws for different fixed-$\theta_{\rm E}$ column and decreases rapidly as the Einstein angle shrinks. The decline in *absolute* cross section is even steeper.

The $\langle\tau\,(>A;K_0)\rangle$ (Eqn 41) and $P\,[\tau\,(>A;K_0)\geq 1]$ (Eqn 3.4) as functions of A for different parameter $K_0 = 16-23$ mag (but tested to be insensitive to the cutoff magnitude $K_c \sim 25-30$ mag), are shown in Figure 12, where $\hat{\sigma}_s \approx 0.5$ for a typical source located at $D_0 + r = 2D_0$ or $\theta_E = \theta_\infty/\sqrt{2}$, for both the total stellar population and the contribution by SMBH alone. E.g. for the threshold of 21 mag, we predict that the probability of seeing in any snapshot of the region around the GC, about one distant background star will be magnified by a factor greater than 5 for 2% of the time, about 1% higher than if there is only the SMBH magnification.

In our results, the net contribution by stars is smaller than that of AL01, this is partly due to the modifica-

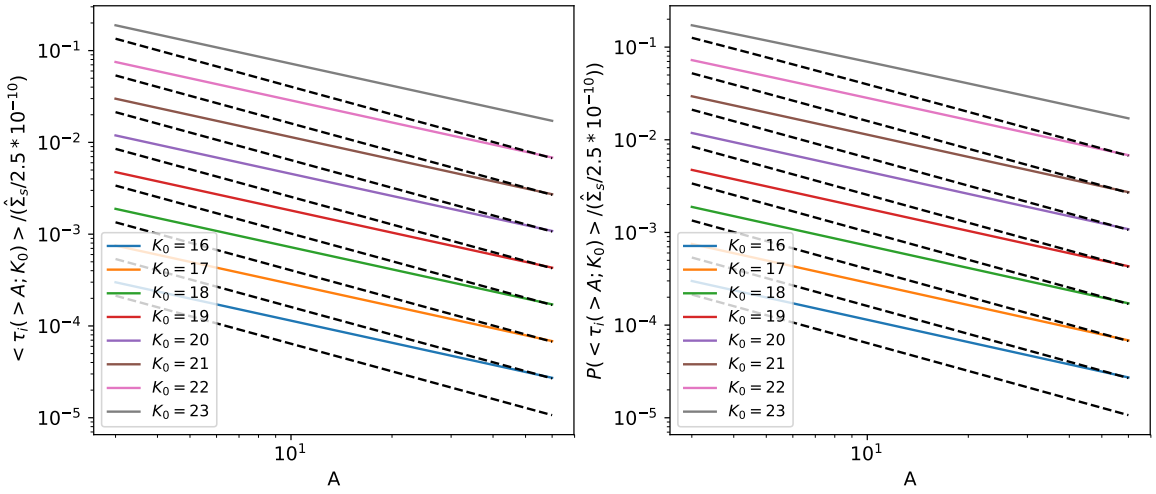

Figure 12. Left: average number of lensed images magnified by more than A that will be observed in the inner $2\theta_E$ with a limiting K-band magnitude K_0, for $D_0 = r$ ($\theta_E = \theta_\infty/\sqrt{2}$) and $b = 0.4$; Right: the fraction of time that at least one lensed image magnified by more than A, will be observed in the inner $2\theta_E$, as functions of A. Dotted line shows the contribution by SMBH alone, detection threshold in magnitude increasing from bottom to top.

tion of the SMBH mass from $3 \times 10^6 M_\odot$ to $4 \times 10^6 M_\odot$ which results in the Einstein radius being farther away from the center, but more importantly the reduction by factor of 5 in a more realistic surface density profile of stars. These events can be identified by their variability and timescale shown in the shapes of complex light-curves (Mao & Paczynski 1991; Gould & Loeb 1992; Wambsganss 1997). The kinematics has been briefly discussed by AL01, they showed that $t(> A)$, the duration of a micro-lensing event with magnification above A, is strongly dependent on the position of image x_{BH} and might be increased from a scale of 10 days to a scale of several months for a secondary lens in the vicinity of the Einstein radius (see Fig 4 of their paper). Theoretically, it is also possible to calculate some sort of a *rate* of events above given magnification threshold not unlike what we did with the GC source micro-lensing in Section 2, but to do that we need an accurate evaluation of the average timescale $\bar{t}$, which brings in complexities in the relative kinematics that we will not go into details in this work.

4. DISCUSSION AND SUMMARY

In this paper we investigated the probabilities of two kinds of microlensing events in the GC, the first being stellar sources within the GC magnified by the SMBH single-lens, and the second being the magnification by SMBH of much more distant sources, with a non-negligible enhancement by the GC stars as secondary lenses. These two categories of events will be generally pronounced at different characteristic Einstein radius of $\sim 0.01''(D_0 >> r)$ and $\sim 1''(D_0 \sim r)$, making them distinguishable from each other by location of observation. In reality, the cases will overlap with each other, and even the magnification of a GC stellar source can also be double-enhanced by its stellar neighbors. However, as shown in Fig 11, the enhancement effect decreases quickly for closer sources with smaller Einstein radius, meaning it's mostly a privilege for distant background stars with the lens and source distance to observer comparable to each other. In another sense, we have shown that the second case will undergo a gradual decay into the first case as the stellar sources get closer to the SMBH lens. We focus on K-band since only IR surveys can peer into the GC and detect such microlensing events.

Our analysis of the first case is based on the methodologies of AS99, who investigated the lensing rates for the K-band stellar sources of the GC core, disk and bulge stars sweeping across the lens plane behind the SMBH. Using newer models updated from observation data including K Luminosity Function (Fig 1), number density profile (Fig 2) and velocity profile (Fig 3), we carried out similar analysis for the stellar population from 0.003pc to 20pc, focusing on the GC which contributes most of the unresolved microlensing rates and avoiding the complexity of involving uncertain models of the galactic disk and bulge. However, we have to point out that the choice of our upper radius 20 pc does affect the calculation of *resolved* lensing rates, since the critical radius d_μ is well outside 20pc for smaller detection thresholds and their only contribution must be from the disk and

bulge stars. In our case, the resolved lensing events of sources inside 20pc would only appear if our telescope is sensitive enough to separate all stellar sources with an apparent magnitude of more than 20 mag.

Comparing our results of unresolved lensing rate (bright stars and faint stars), rate-averaged amplification and timescale, as well as the differential rate contributed by sources with certain distance with AS99, we find that our results follow slightly different profiles but similar to good order. The main differences are that our total lensing rate is generally smaller by a factor of 2 with the long timescale lensing rate decreasing slower as ΔT, the time for sampling interval increases, and our rate-averaged amplification $\overline{\Delta K}$ is generally larger ($\sim 1-2$ mag) and converges more slowly to its asymptotic value of 0.75 mag at small ΔT. The possible mechanisms that results in the difference is discussed in §2.7. Generally, the lensing rates increase as our observation threshold extend to lower luminosity. The results are presented in a practical way so that we can look up the graph and calculate the probability of detecting an event for an arbitrarily long monitoring campaign with given detection interval between runs ΔT, for example, a campaign carried out with sampling interval $\Delta T = 1$yr and threshold $K_0 = 19$ mag will give a rate of 5×10^{-3} per year for long events subject to multiple monitoring with a characteristic amplification of 1 magnitude. For shorter events that would only appear as a "flash" in one of the observations, the rate would be 4×10^{-3} per year and the average timescale of such events would be $\sim$ 70 days. Such a campaign carried out for 10 years will give 0.06 events on average.

Still, the previous case only corresponds to very small separation $\theta_{\rm E} \sim 0.01''$, while lensing events of the second case are on a larger scale and easier to detect. In our analysis of the second scenario, we followed the methodologies of AL01. We prove that the optical depth can be effectively calculated using mean stellar mass, and we use a new and more realistic stellar surface density model that is consistent with our previously applied stellar density Nuker model as well as observations to obtain an enhancement effect smaller than AL01. We predict that the probability of seeing at least one distant background star magnified above a factor of 5 around the inner $2\theta_{\rm E} \sim 3''$ to be 2% given a modern detection threshold of $\sim$ 21 mag, and therefore in any K-band snapshot of the region around the GC, about one distant background star will be magnified by a factor greater than 5 for 2% of the time.

More importantly, the light-curves of such events will be considerably altered by the gravitational shear, and will reveal much information on the property of the source as well as the lens (Paczynski 1986; Mao & Paczynski 1991; Gould & Loeb 1992), which can help probe the profiles of stars beyond the current detection limit. We point out that a non-negligible fraction of the net optical depth is contributed by SBHs as secondary lenses, therefore this method can be used to search for SBHs and study the mass segregation in the GC. We also want to point out that all the above discussions can be applied to other galaxies harboring a SMBH surrounded by a dense stellar cusp as well as planetary system with a dense asteroid population, these systems will have different characteristic secondary-to-primary lens mass ratio ϵ (e.g. Bozza et al. 2008).

In recent years numerous microlensing campaigns towards the galactic bulge have been carried out (e.g Afonso et al. 2003; Navarro et al. 2017; Mróz et al. 2019). However, most of them are at optical wavelengths and cannot probe into the GC. Meanwhile, modern AO surveys in K-band luminosity can probe into the GC central arcsec with high precision. We believe that with more potential microlensing events discovered and recorded, we would be able to compare them with our predictions and provide more information on the GC and the SMBH.

We must clarify that our working model of distant background sources from AL01 is subject to a lot of uncertainties (extinction in the galactic plane, distribution of star-forming regions in the spirals behind GC, etc) and calls for improvement. Also in this paper we didn't consider any other lenses than the SMBH, such as the dense population of SBHs with non-negligible contribution in generating microlensing events in the GC central arc-sec (Chanamé et al. 2001). More precise calculation with modified methods that can treat more complicated anisotropic velocity dispersions is left for future work.

ACKNOWLEDGMENTS

We thank Shude Mao and Hagai Peret for helpful discussions. Y. X. C. thanks the Department of Astronomy of U.C. Berkeley its hospitality during his semester of exchange in California, partially sponsored by the Tsinghua Xuetang Cultivation Program.

APPENDIX

A. THE TRADITIONAL WAY TO DERIVE FOR THE DIFFERENTIAL LENSING RATE AND A NEW INTERPRETATION

To derive the expression for lensing-rate of the stellar contribution integrated through thin "slabs" with distance to SMBH r and of thickness dr (Eqn 9), there are multiple approaches we can use.

Conventionally, Mao & Paczynski (1991); Kiraga & Paczynski (1994) gave the average rate for a lensing event of Einstein crossing time t_E, assumed detection threshold $u_{max} = 1$ and stellar source optical depth τ to be $\Gamma = (\overline{\Delta t})^{-1}$ Where average interval between events is

$$\overline{\Delta t} = \frac{\pi t_E}{2\tau}, \tag{A1}$$

where in our case $t_{\rm E} = R_{\rm S}/v_{2D}$ is the Einstein crossing time for a given source mass with velocity v_{2D} (The collective behavior for an isotropic Gaussian distribution of v_{2D} is a simple generalization). This can be obtained by averaging over the timescales of lensing events to get

$$\bar{t} = \overline{2t_E\sqrt{1-u_0^2}} = \int_0^1 2t_E\sqrt{1-u_0^2}P(u_0)du_0 = \frac{\pi}{2}t_E \tag{A2}$$

Where $P(u_0)$ is the probability distribution over different u_0, usually assumed to be

$$P(u_0 = x) = 1, 0 < x < 1$$

and the average interval (averaging over impact parameter) will be the average timescale over optical depth $\overline{\Delta t} = \bar{t}/\tau$.

If we use this expression to calculate the lensing rate, for the slab of thickness dr and circular area $\pi(u_{max}R_S)^2 \approx \pi(u_{max}R_E)^2$ also for $u_{max} = 1$ (same method applies for arbitrary u_{max}), we will have:

$$\overline{d\Gamma} = \frac{\tau}{\bar{t}} = \frac{2(\tau = \pi R_E^2 dr n_*)}{\pi t_E} = 2R_E v_{2D} n_* dr \tag{A3}$$

For the differential contribution by a certain impact parameter u_0, we can still obtain it according to expression $\overline{\Delta t} = \bar{t}/\tau$, but for a specific timescale/impact parameter, the optical depth should be calculated from two STRIPS across a disk, with total volume $2 \times 2R_E\sqrt{1-u_0^2}du_0R_Edr$ instead of $\pi R_E^2 dr$. For these events, the timescale is fixed to $2t_E\sqrt{1-u_0^2}$, and

$$\frac{d\Gamma}{du_0} = P(u_0)\frac{4R_E^2\sqrt{1-u_0^2}du_0 dr n_*}{2t_E\sqrt{1-u_0^2}}/du_0 = P(u_0)2R_E v_{2D} n_* dr \tag{A4}$$

So the differential distribution for du_0 is the same as the total rate. This expression is adopted by Mróz et al. (2019); Peale (1998); Mao & Paczynski (1996) for lensing rate produced by fixed source with a distribution of potential lens and have implicitly assumed $P(u_0) = 1$.

Another more visual way to calculate the expressions is to take the area perpendicular to 2-D velocity viewing the *side* of the slab edge-on (to see a rectangle of length $2u_{max}R_{\rm E}$ and width dr) and count how many sources goes through it per unit time. When the distribution over u_0 is uniform, this thin slit gives an effective projected area of impact $A = 2R_{\rm E}dr$, and by $n\sigma v$ calculation the rate is naturally

$$\overline{d\Gamma} = n_* \cdot A \cdot v = n_* 2R_E v_{2D} dr \tag{A5}$$

This is for $P(u_0) = 1$. For arbitrary $P(u_0)$, the contribution by a specific u_0 only has effective projected area of impact $dA = 2du_0R_Edr$ consisting of two small rectangular HOLES, so the differential contribution is

$$\frac{d\Gamma}{du_0} = P(u_0)n_* \cdot dA \cdot v/du_0 = P(u_0)n_* 2R_E v_{2D} dr \tag{A6}$$

This differential contribution formula can be utilized to apply some selection rules on u_0.

Nevertheless, should we follow the assumption of $P(u_0) = 1$ with no dependence on crossing velocity, we would be able to generalize Eqn A5 for the luminosity-related $u_{max}(K_s)$ and the velocity distribution $DF_2(v_{2D})d^2v_{2D}$ to calculate the local rate contributed by sources within certain luminosity bin $df(K_s)$ and at certain distance r:

$$\frac{d^2\Gamma}{drdf} = u_{max}(K_s)n_*(r)2R_E(r)\int_0^{v_{max}} DF_2(v_{2D})d^2v_{2D}. \tag{A7}$$

For continuous monitering $v_{max} = \infty$ has no dependence on luminosity, and the integration outcome of $\int_0^{v_{max}} DF_2(v_{2D})d^2v_{2D}$ yields the mean velocity $\int_0^{\infty} DF_2(v_{2D})d^2v_{2D} = \overline{v_{2D}(r)}$ only related to distance r (as our model assumption), and we arrive at Eqn 11.

REFERENCES

Afonso, C., Albert, J. N., Alard, C., et al. 2003, A&A, 404, 145, doi: 10.1051/0004-6361:20030307

Aharon, D., & Perets, H. B. 2016, ApJL, 830, L1, doi: 10.3847/2041-8205/830/1/L1

Alard, C., Guibert, J., Bienayme, O., et al. 1995, The Messenger, 80, 31

Alexander, T., & Hopman, C. 2009, ApJ, 697, 1861, doi: 10.1088/0004-637X/697/2/1861

Alexander, T., & Loeb, A. 2001, ApJ, 551, 223, doi: 10.1086/320087

Alexander, T., & Sternberg, A. 1999, ApJ, 520, 137, doi: 10.1086/307446

Bahcall, J. N., & Wolf, R. A. 1976, ApJ, 209, 214, doi: 10.1086/154711

Bartko, H., Martins, F., Trippe, S., et al. 2010, ApJ, 708, 834, doi: 10.1088/0004-637X/708/1/834

Baumgardt, H., Amaro-Seoane, P., & Schödel, R. 2018, A&A, 609, A28, doi: 10.1051/0004-6361/201730462

Blum, R. D., Sellgren, K., & Depoy, D. L. 1996, ApJ, 470, 864, doi: 10.1086/177917

Bozza, V., Calchi Novati, S., & Mancini, L. 2008, ApJ, 675, 340, doi: 10.1086/525271

Chanamé, J., Gould, A., & Miralda-Escudé, J. 2001, ApJ, 563, 793, doi: 10.1086/323986

Chatzopoulos, S., Fritz, T. K., Gerhard, O., et al. 2015, MNRAS, 447, 948, doi: 10.1093/mnras/stu2452

Do, T., Lu, J. R., Ghez, A. M., et al. 2013, ApJ, 764, 154, doi: 10.1088/0004-637X/764/2/154

Do, T., Hees, A., Ghez, A., et al. 2019, Science, 365, 664, doi: 10.1126/science.aav8137

Dong, S., Mérand, A., Delplancke-Ströbele, F., et al. 2019, ApJ, 871, 70, doi: 10.3847/1538-4357/aaeffb

Eisenhauer, F., Genzel, R., Alexander, T., et al. 2005, ApJ, 628, 246, doi: 10.1086/430667

Emami, R., & Loeb, A. 2020, JCAP, 2020, 021, doi: 10.1088/1475-7516/2020/02/021

Feldmeier, A., Neumayer, N., Seth, A., et al. 2014, A&A, 570, A2, doi: 10.1051/0004-6361/201423777

Fritz, T. K., Chatzopoulos, S., Gerhard, O., et al. 2016, ApJ, 821, 44, doi: 10.3847/0004-637X/821/1/44

Gallego-Cano, E., Schödel, R., Dong, H., et al. 2018, A&A, 609, A26, doi: 10.1051/0004-6361/201730451

Gautam, A. K., Do, T., Ghez, A. M., et al. 2019, ApJ, 871, 103, doi: 10.3847/1538-4357/aaf103

Genzel, R., Eckart, A., Ott, T., & Eisenhauer, F. 1997, MNRAS, 291, 219, doi: 10.1093/mnras/291.1.219

Genzel, R., Eisenhauer, F., & Gillessen, S. 2010, Reviews of Modern Physics, 82, 3121, doi: 10.1103/RevModPhys.82.3121

Genzel, R., Thatte, N., Krabbe, A., Kroker, H., & Tacconi-Garman, L. E. 1996, ApJ, 472, 153, doi: 10.1086/178051

Ghez, A. M., Klein, B. L., Morris, M., & Becklin, E. E. 1998, ApJ, 509, 678, doi: 10.1086/306528

Ghez, A. M., Salim, S., Weinberg, N. N., et al. 2008, ApJ, 689, 1044, doi: 10.1086/592738

Gillessen, S., Eisenhauer, F., Trippe, S., et al. 2009, ApJ, 692, 1075, doi: 10.1088/0004-637X/692/2/1075

Gould, A., & Loeb, A. 1992, ApJ, 396, 104, doi: 10.1086/171700

Gravity Collaboration, Abuter, R., Amorim, A., et al. 2020, A&A, 636, L5, doi: 10.1051/0004-6361/202037813

Hopman, C., & Alexander, T. 2006, ApJL, 645, L133, doi: 10.1086/506273

Kiraga, M., & Paczynski, B. 1994, ApJL, 430, L101, doi: 10.1086/187448

Lam, C. Y., Lu, J. R., Hosek, Matthew W., J., Dawson, W. A., & Golovich, N. R. 2020, ApJ, 889, 31, doi: 10.3847/1538-4357/ab5fd3

Lauer, T. R., Ajhar, E. A., Byun, Y. I., et al. 1995, AJ, 110, 2622, doi: 10.1086/117719

Lu, J. R., Do, T., Ghez, A. M., et al. 2013, ApJ, 764, 155, doi: 10.1088/0004-637X/764/2/155

Lu, J. R., Ghez, A. M., Hornstein, S. D., et al. 2009, ApJ, 690, 1463, doi: 10.1088/0004-637X/690/2/1463

Mao, S., & Paczynski, B. 1991, ApJL, 374, L37, doi: 10.1086/186066

—. 1996, ApJ, 473, 57, doi: 10.1086/178126

McGinn, M. T., Sellgren, K., Becklin, E. E., & Hall, D. N. B. 1989, ApJ, 338, 824, doi: 10.1086/167239

Miralda-Escudé, J., & Gould, A. 2000, ApJ, 545, 847, doi: 10.1086/317837

Mróz, P., Udalski, A., Skowron, J., et al. 2019, ApJS, 244, 29, doi: 10.3847/1538-4365/ab426b

Navarro, M. G., Minniti, D., & Contreras Ramos, R. 2017, ApJL, 851, L13, doi: 10.3847/2041-8213/aa9b29

Paczynski, B. 1986, ApJ, 304, 1, doi: 10.1086/164140

—. 1996, ARA&A, 34, 419, doi: 10.1146/annurev.astro.34.1.419
Peale, S. J. 1998, ApJ, 509, 177, doi: 10.1086/306490
Pfuhl, O., Fritz, T. K., Zilka, M., et al. 2011, ApJ, 741, 108, doi: 10.1088/0004-637X/741/2/108
Rafelski, M., Ghez, A. M., Hornstein, S. D., Lu, J. R., & Morris, M. 2007, ApJ, 659, 1241, doi: 10.1086/512062
Schöck, M., Els, S., Riddle, R., et al. 2009, PASP, 121, 384, doi: 10.1086/599287
Schödel, R., Gallego-Cano, E., Dong, H., et al. 2018, A&A, 609, A27, doi: 10.1051/0004-6361/201730452
Schödel, R., Merritt, D., & Eckart, A. 2009, A&A, 502, 91, doi: 10.1051/0004-6361/200810922
Schödel, R., Eckart, A., Alexander, T., et al. 2007, A&A, 469, 125, doi: 10.1051/0004-6361:20065089
Støstad, M., Do, T., Murray, N., et al. 2015, ApJ, 808, 106, doi: 10.1088/0004-637X/808/2/106
Sumi, T., & Penny, M. T. 2016, ApJ, 827, 139, doi: 10.3847/0004-637X/827/2/139
Sumi, T., Bennett, D. P., Bond, I. A., et al. 2013, ApJ, 778, 150, doi: 10.1088/0004-637X/778/2/150
Udalski, A., Szymanski, M., Kaluzny, J., et al. 1993, AcA, 43, 289
Wambsganss, J. 1997, MNRAS, 284, 172, doi: 10.1093/mnras/284.1.172
Wardle, M., & Yusef-Zadeh, F. 1992, ApJL, 387, L65, doi: 10.1086/186306
Wiktorowicz, G., Wyrzykowski, Ł., Chruslinska, M., et al. 2019, ApJ, 885, 1, doi: 10.3847/1538-4357/ab45e6